nature photonics

ARTICLES

https://doi.org/10.1038/s41566-020-0631-z

Check for updates

Monitoring contractility in cardiac tissue with cellular resolution using biointegrated microlasers

Marcel Schubert[1,2]✉, Lewis Woolfson[1], Isla R. M. Barnard[1], Amy M. Dorward[3], Becky Casement[1], Andrew Morton[1], Gavin B. Robertson[3], Paul L. Appleton[4], Gareth B. Miles[2,5], Carl S. Tucker[6], Samantha J. Pitt[2,3] and Malte C. Gather[1,2,7]✉

The contractility of cardiac cells is a key parameter that describes the biomechanical characteristics of the beating heart, but functional monitoring of three-dimensional cardiac tissue with single-cell resolution remains a major challenge. Here, we introduce microscopic whispering-gallery-mode lasers into cardiac cells to realize all-optical recording of transient cardiac contraction profiles with cellular resolution. The brilliant emission and high spectral sensitivity of microlasers to local changes in refractive index enable long-term tracking of individual cardiac cells, monitoring of drug administration, accurate measurements of organ-scale contractility in live zebrafish, and robust contractility sensing through hundreds of micrometres of rat heart tissue. Our study reveals changes in sarcomeric protein density as an underlying factor to cardiac contraction. More broadly, the use of novel micro- and nanoscopic lasers as non-invasive, biointegrated optical sensors brings new opportunities to monitor a wide range of physiological parameters with cellular resolution.

An estimated 26 million patients suffer from heart failure worldwide and further advances in cardiac regeneration depend critically on the ability to locally resolve the contractile properties of heart tissue[1,2]. Currently available techniques lack speed, sensitivity and single-cell specificity, especially in deep tissue. To monitor cardiac contractility in isolated cells in a culture dish, transmission or fluorescence microscopy is often sufficient to track the distinct structural features of myofibrils[3], cellular organelles that comprise repeating contractile elements called sarcomeres. However, characterizing contractility with adequate resolution in the more complex three-dimensional (3D) structures of cardiac tissue remains a major challenge—both in vitro and in vivo—mainly due to the fast dynamics of contractions (<50 ms), the strong motion of the tissue and the severe scattering of light in tissue. Force transducers or soft strain gauge sensors have been developed, but their spatial resolution is very limited[4]. In transparent zebrafish, light-sheet microscopes in combination with image reconstruction algorithms allow volumetric imaging of whole hearts with single-cell resolution[5]; however, their resolution is too low to extract the contractility of single cells as this requires tracking nanometre changes in sarcomere spacing[2]. Fast intravital scanning confocal or multiphoton microscopes have been developed to achieve this resolution but the need for extensive image artefact removal by retrospective gating, active tissue stabilization and targeted fluorescent labelling means that so far they can only extract averaged contraction profiles. Furthermore, due to the inherent tissue dynamics, progress in achievable imaging depth has stalled at less than 100 µm from the heart surface[1,2,6,7], which is in sharp contrast to functional imaging of the brain, which has recently reached a depth of 850 µm (ref. [8]).

We explored the integration of whispering gallery mode (WGM) microlasers as multifunctional optical sensors to elucidate cardiomyocyte contractility under various experimental conditions. Chip-based fibre- and prism-coupled WGM biosensors have previously achieved sensitivities down to the single molecule and protein level[9,10]. However, their potential for intracellular sensing remains largely unexplored as integration into biological systems requires further miniaturization, self-sustained and prolonged emission of light, and data analysis protocols with improved robustness. Microlasers were recently proposed as novel optical tags to uniquely discriminate hundreds of thousands of cells[11–15].

Intracellular refractive index sensing

Figure 1 illustrates the general principle of our laser-based contraction sensor. Brightly fluorescent polystyrene microspheres with diameters between 10 and 20 µm were used as efficient and robust microscopic WGM lasers that show multimode emission under remote optical pumping[11]. These lasers were actively internalized by different types of cardiac cells (Supplementary Fig. 1 and Supplementary Information). Following cardiomyocyte contraction, individual peaks in the emission spectrum of the lasers showed a spectral redshift (typically, $\Delta\lambda \approx 50$ pm; Fig. 1d). Due to the bright and narrow-band laser emission, the wavelength of each lasing mode can be monitored rapidly (acquisition rate, 100 Hz) and accurately (spectral resolution, 1 pm), revealing pulse-shaped perturbations in lasing wavelength that are synchronized across all modes and coincident with the spontaneous contractions of the cell (Fig. 2a,b and Supplementary Video 1). By tracking at least two pairs of transverse electric and transverse magnetic lasing modes and fitting their positions to an optical model, we independently determined the diameter of each microsphere and the average external refractive index (n_{ext}); that is, the refractive index of the volume probed by the evanescent component of the WGM (Fig. 2c,

[1]SUPA, School of Physics and Astronomy, University of St Andrews, St Andrews, UK. [2]Centre of Biophotonics, University of St Andrews, St Andrews, UK. [3]School of Medicine, University of St Andrews, St Andrews, UK. [4]School of Life Sciences, University of Dundee, Dundee, UK. [5]School of Psychology and Neuroscience, University of St Andrews, St Andrews, UK. [6]The Queen's Medical Research Institute, University of Edinburgh, Edinburgh, UK. [7]Present address: Centre for Nanobiophotonics, Department of Chemistry, University of Cologne, Cologne, Germany. ✉e-mail: ms293@st-andrews.ac.uk; mcg6@st-andrews.ac.uk

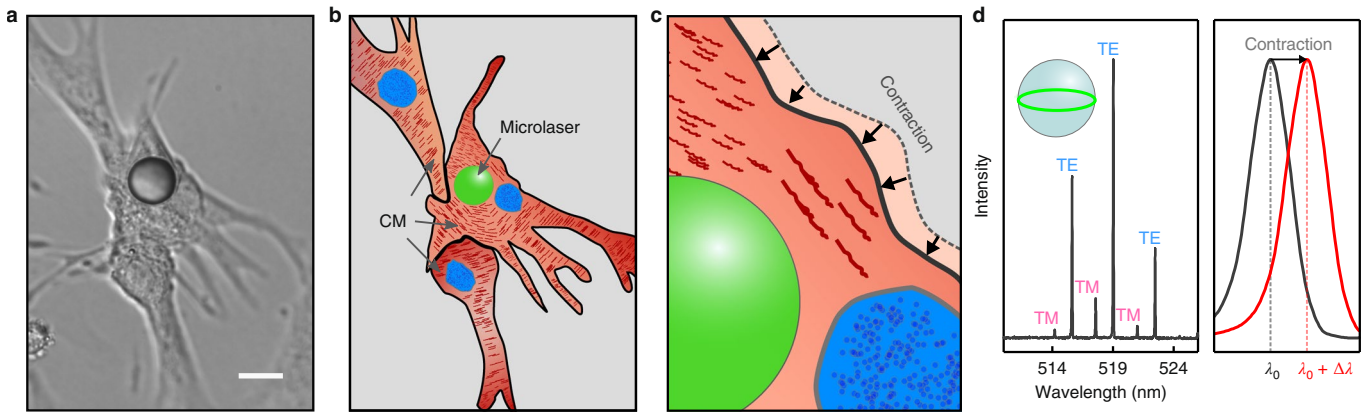

Fig. 1 | The principle of microlaser-based intracellular sensing in neonatal mouse cardiomyocytes. a,**b**, A differential interference contrast (DIC) microscopy image (**a**) and a schematic illustration (**b**) of a group of neonatal cardiomyocytes (CM; nuclei indicated in blue) with an intracellular microlaser (green sphere). **c**, A magnified view that visualizes the contractile movement of the cell around the microlaser due to the action of sarcomeres (dark red fibres). **d**, Left: a measured WGM spectrum of a microlaser showing multimode lasing in pairs of TE- and TM-modes; the WGMs are localized in an equatorial plane close to the surface of the microlaser (inset, green line). Right: a magnification of one peak in the WGM spectrum that illustrates the redshift in the lasing wavelength following cardiomyocyte contraction ($\lambda_0 = 519$ nm, $\Delta\lambda = 50$ pm). Scale bar, 15 μm.

Supplementary Fig. 2 and the Supplementary Information). This revealed a characteristic increase in the refractive index during cell contractions. Statistical analysis of the microsphere diameter was then applied to reduce the effect of fitting noise before reiterating the refractive index calculation. This substantially improved the signal quality and thus allowed the detection of minute changes in n_{ext}, with a refractive index resolution of 5×10^{-5} (Supplementary Information), which rivals the most sensitive cell refractometric techniques that are currently available[16].

Of the two pairs of transverse electric and transverse magnetic lasing modes that are required for fitting to the optical model, the brightest mode typically has a lasing threshold well below 1 mJ cm^{-2} (which corresponds to <1 nJ per pulse, Fig. 2d). Above this threshold, this mode rapidly increased in intensity to become orders of magnitude more intense than the background, which is mostly formed by bulk fluorescence of the microlaser (signal-to-background ratio, SBR > 15 dB). Single-pulse excitation at around 1–2 mJ cm^{-2} can therefore be used to accurately determine the spectral position of this mode (Supplementary Fig. 3). By comparison, the least intense mode of the two pairs required 10 to 50 times higher pump energy to pass the lasing threshold and to determine its spectral position with sufficient accuracy to ensure convergence of our fitting algorithm. Furthermore, we found that the periodic changes in refractive index due to cardiomyocyte contraction can be utilized to determine the sensitivity of each laser mode (Fig. 2e, Supplementary Fig. 4 and Supplementary Information). Using the sensitivity and tracking the spectral position of just the brightest lasing mode then allows calculation of a linearly approximated external refractive index, n^*_{ext}, reducing the minimum required pump energy by at least one order of magnitude. This calibration protocol enabled real-time refractive index sensing, allowed continuous yet non-disruptive readout (Fig. 2f) and greatly improved the robustness of the approach under challenging experimental conditions (see below).

Analysis of multiple cardiomyocytes revealed that contractions consistently led to an increase of cellular refractive index, which indicates the presence of a reproducible physiological process that alters the optical properties of cardiomyocytes depending on the activation state of their contractile elements (Fig. 2g).

Microlasers monitor myofibril contractility

We analysed the 3D organization of myofibrils to identify the origin of the refractive index increase during cardiomyocyte contraction. It is generally assumed that cardiomyocytes contract under isovolumetric conditions[17], yet X-ray diffraction experiments have revealed a linear relationship between sarcomere length and the volume of the myofibril unit cell, indicating that cell contractions significantly increase the protein density of the myofibrils[18]. Three dimensional reconstructions of cells showed that microlasers are surrounded by—and in direct contact with—a dense network of myofibrils (Fig. 3a–c, Supplementary Fig. 5), indicating a strong overlap of the contractile protein machinery with the evanescent field of the laser mode, which typically extends up to 200 nm above the resonator surface. Cellular contractility in neonatal cardiomyocytes was then measured by staining sarcomeric actin filaments and tracking their length change during the contraction cycle while simultaneously recording spectral shifts in microlaser emission (Fig. 3d,e and Supplementary Video 2). We find that the shortening in the sarcomere length of myofibrils was linearly correlated to n_{ext} (Supplementary Fig. 6). By contrast, we did not observe spectral shifts for microlasers located inside cardiomyocytes that were not actively beating even when these were in direct contact with a contracting neighbouring cell, confirming the very localized nature of evanescent field sensing. This indicates that structural changes inside contracting myofibrils cause the redshift in lasing wavelength. Given that during systole n_{ext} increased by up to 0.003, and using the known protein refractive index increment (dn/dc, where n is the refractive index of a protein containing sample and c is the protein concentration), we further estimated that the observed contraction-induced changes in sarcomere length by about 10% led to a maximum increase in protein concentration of approximately 8% (Supplementary Information). This finding is consistent with the previously reported decrease in unit cell volume[18]. It does not contradict observations that the contraction of the whole heart is isovolumetric; during contraction, cardiac cells are likely to expel water from the myofibrils into different parts of the cell or to the extracellular space[19], causing a local increase in myofibril density while still conserving the overall tissue volume. The effects associated with sarcomeric lattice spacing and unit cell changes are of great importance for the function of cardiac cells and are believed to play an important role in regulating the length-dependent activation of the heart (Frank–Starling law). As transient refractive index profiles provide a direct measure of cardiomyocyte contractility and myofibril density, they provide new insights to the mechanobiology of cardiac cells. Importantly, the signal monitored by the microlaser

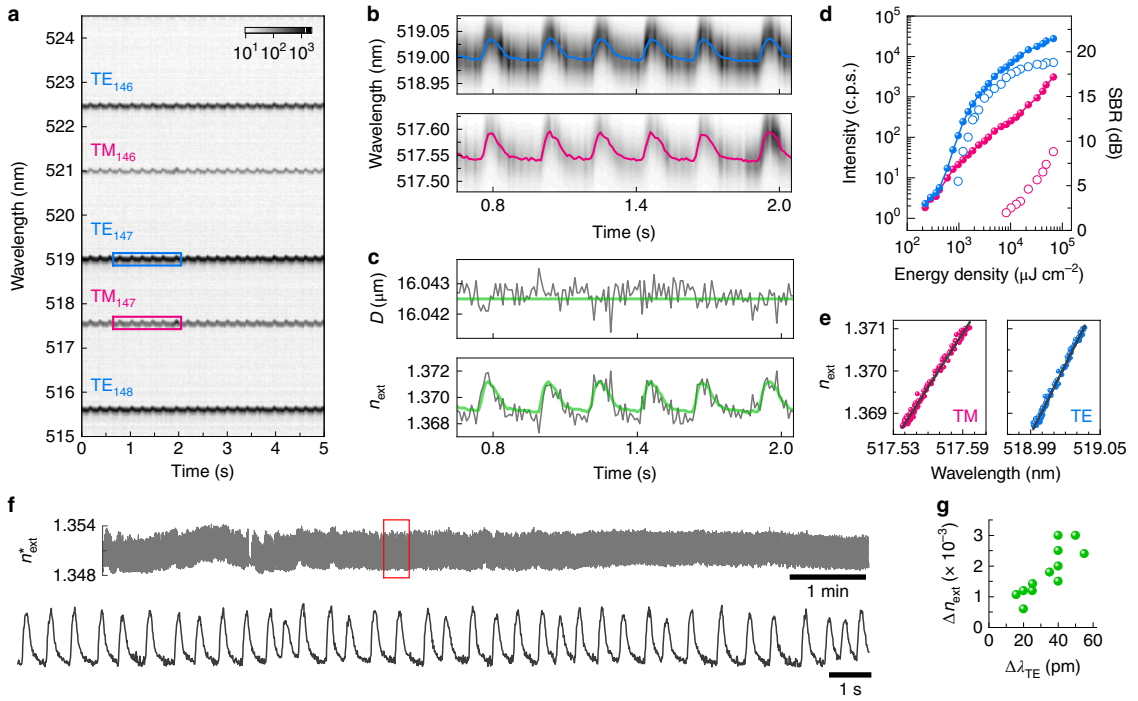

Fig. 2 | Transient redshifts of microlaser emission are caused by changes in the intracellular refractive index. a, A contour plot of the temporal evolution of the lasing spectra for an intracellular microlaser, measured at 10 ms temporal resolution. **b**, A magnified view of the areas highlighted in **a** for a pair of transverse electric (TE, blue) and transverse magnetic (TM, pink) WGMs with angular mode number 147. The coloured lines show the centre position of each mode obtained from peak fitting. Shifts to longer wavelengths coincide with spontaneous cardiomyocyte contractions. **c**, Top: the calculated diameter (D) of the microlaser (grey) and mean diameter (green). Bottom: n_{ext} calculated with an unrestricted microlaser diameter (grey) and by applying the fixed mean diameter of the microlaser (green). **d**, The typical threshold characteristics (left axis, closed symbols) for the brightest TE mode (blue) and the least intense TM mode (pink) of four tracked lasing modes. Lasing thresholds are about 500 μJ cm^{-2} (TE) and 20 mJ cm^{-2} (TM). The SBR (right axis, open symbols) of the same modes under single-pulse excitation. c.p.s., counts per second. **e**, Calibration of the two modes shown in **b** using data from six contractions. Sensitivities of 0.0429 nm^{-1} and 0.0549 nm^{-1} are obtained from the slope of the linear fit (grey line) for the TM and TE modes, respectively. **f**, Continuous single-cell monitoring over 10 min (top) at 2 mJ cm^{-2} (corresponding to 2 nJ per pulse) and a magnified view of the 20 s window indicated by the red rectangle (bottom). **g**, The average external refractive index change (Δn_{ext}) between resting phase (diastole) and peak contraction (systole) for $n=12$ cells plotted against the corresponding average change of the dominant TE WGM ($\Delta\lambda_{TE}$). Data are representative of more than 20 independent repeats for a total of $n>150$ cells.

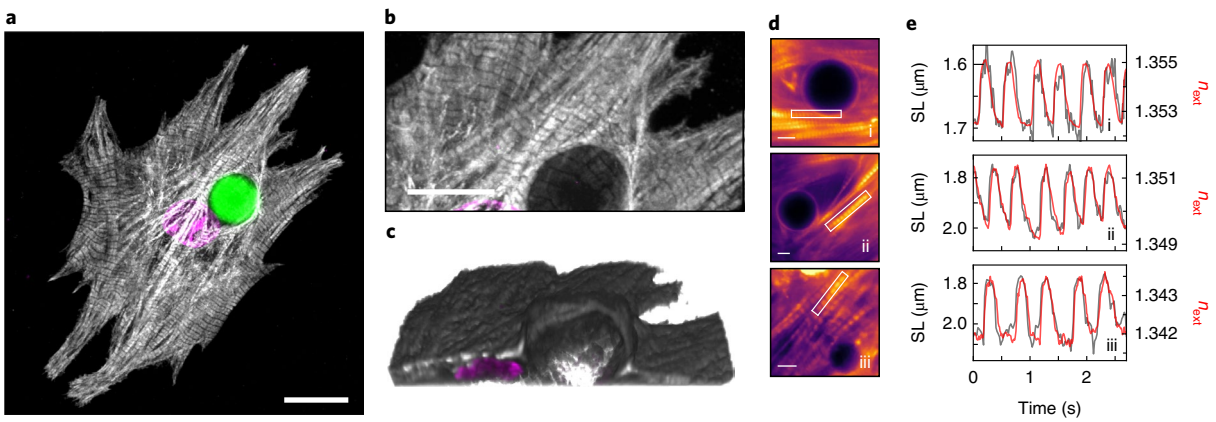

Fig. 3 | Microlasers monitor cellular contractility. 3D arrangement of myofibrils around microlasers in neonatal cardiomyocytes. **a**, A confocal microscopy maximum-intensity projection that shows the sarcomeric protein cardiac troponin T (grey), cell nucleus (magenta) and microlaser (green). Scale bar, 15 μm. **b**,**c**, A magnification of the region around the microlaser (**b**) and a 3D reconstruction of the same area (**c**). The microlaser is omitted to show the arrangement of the myofibrils more clearly. Scale bar, 10 μm. **d**, Video-rate epifluorescence microscopy images (Supplementary Video 2) of neonatal mouse cardiomyocytes with labelled myofibrils. Intracellular microlasers are visible as dark circular objects. Scale bars, 5 μm. **e**, Simultaneously acquired temporal profiles of sarcomere length (SL; grey, left axis, extracted from fluorescence profiles of the myofibrils highlighted by the white rectangles in **d**) and n_{ext} (red, right axis, extracted from microlaser spectra). The subfigures (i), (ii) and (iii) are labelled according to the images in **d**.

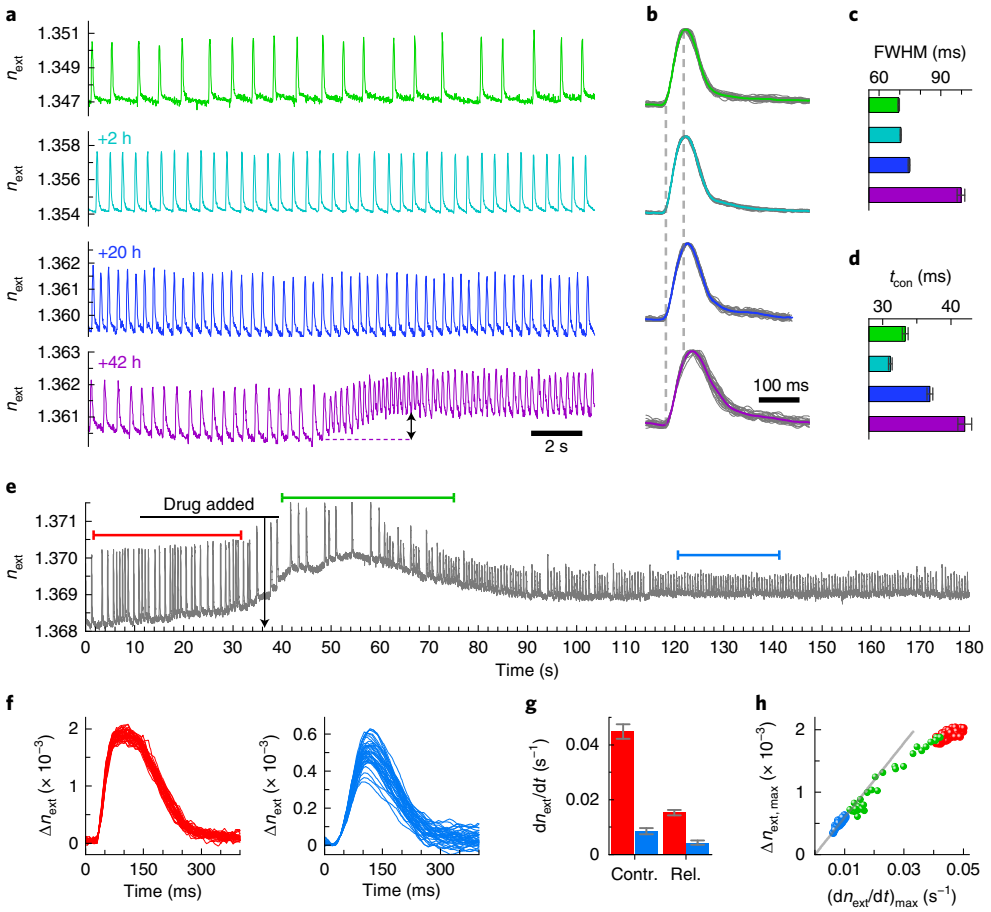

Fig. 4 | Single-cell tracking and contractility sensing under compromised conditions. a–d, Microlaser-based tracking and monitoring of a single neonatal cardiomyocyte. **a**, The intracellular n_{ext} trace (green) of an individual cardiomyocyte at the start of experiment, and characterized again after 2 h (cyan), 20 h (blue) and 42 h (violet). The black double-headed arrow indicates increased contractility during spontaneous tachycardia. **b**, Normalized n_{ext} profiles of traces shown in **a** for $n = 30$–40 cell contractions (grey lines), overlaid by the averaged n_{ext} profiles (coloured lines). Vertical grey dashed lines are a guide to the eye. **c**,**d**, Full-width at half-maximum (FWHM) (**c**) and average contraction time (t_{con}) (**d**) of the beating profiles in **b**. **e**–**h**, The effect of nifedipine on single-cell contractility. **e**, n_{ext} trace of a spontaneously beating neonatal cardiomyocyte during administration of 500 nM nifedipine (black arrow). **f**, Δn_{ext} profiles of individual contractions recorded before (left, red bar in **e**) and after (right, blue bar in **e**) administration of nifedipine. **g**, The average maximum speed of contraction (contr.) and relaxation (rel.) for the beating profiles shown in **f**. **h**, The maximum refractive index change, $\Delta n_{ext,max}$, plotted as a function of the maximum contraction speed. The intermediate region (green bar in **e**) is also shown. The grey line represents a linear fit to the data after equilibration of the cell (blue spheres). All error bars represent the s.e.m.

closely matches the contractility dynamics of nearby cells (Supplementary Fig. 7, Supplementary Video 3), indicating that the functional properties of neonatal cardiomyocytes are not affected by the presence of the microlasers.

Single-cell barcoding

As the microlaser size provides a unique label for identifying and tracking individual cells over time (Supplementary Fig. 8)[11,12], we were able to perform repeated monitoring of single neonatal cardiomyocytes (Fig. 4a). Normalized contractility profiles (Fig. 4b) showed high temporal regularity with minimal beat-to-beat variations in pulse width (full-width at half maximum, Fig. 4c) and contraction time (t_{con}, Fig. 4d). In addition, after 42 h we observed a spontaneous transition into tachycardia (Fig. 4a) that is typically accompanied by increased myocardial tension at elevated beating rates (Bowditch effect), a fundamental process underlying the force–frequency relationship of the heart[20]. At the cellular level this is caused by increased contractility, which we detected as a step-like increase in the maximum and baseline n_{ext} (black arrow in Fig. 4a), allowing simple quantification of relative protein density changes during the entire contraction cycle.

Monitoring drug administration

Next we used the quantitative refractive index transient provided by our laser sensors to assess the effect of the calcium channel blocker nifedipine (Fig. 4e). Although the effect of nifedipine on voltage-gated Ca^{2+}-channels and subsequent intracellular Ca^{2+} dynamics is well documented[21,22], the effect on contractility is less well understood as it is difficult to access in neonatal and stem-cell-derived cardiomyocytes. After administration of nifedipine and following a short period of adaptation, spontaneously beating neonatal cardiomyocytes showed strongly reduced contraction and relaxation speeds (Fig. 4f,g). Furthermore, although we observed that nifedipine increased the pulse-to-pulse variability in Δn_{ext}, the time to reach the maximum contraction changed only marginally (Fig. 4f). The lower contraction speed was therefore largely caused by a reduced contractility of the cell. Under these compromised conditions, the relationship between the mechanical dynamics (contraction speed) and the maximum density change a cell can produce ($\Delta n_{ext,max}$) was linear (Fig. 4h, Supplementary Fig. 9). The nanoscopic probe volume of microlasers and the quantitative contractility information they provide therefore offer insights into fundamental biomechanical processes of cardiac cells, for example revealing links between

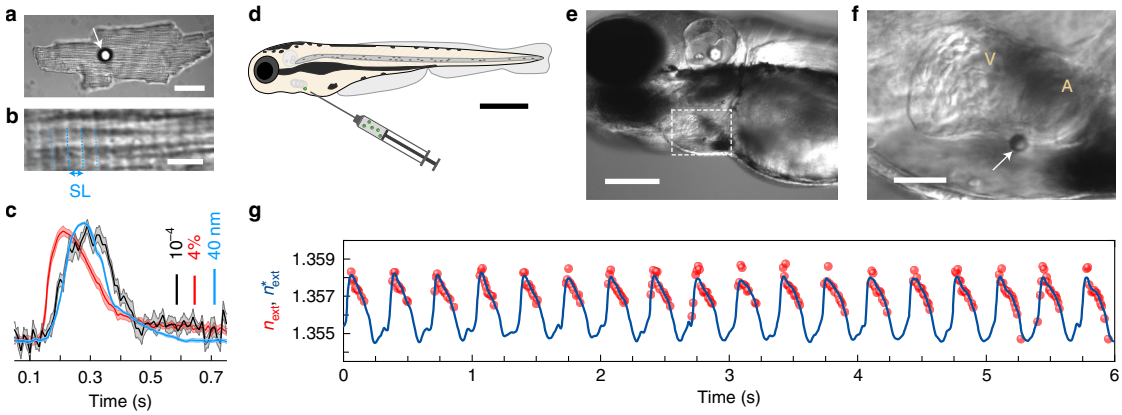

Fig. 5 | Multimodal sensing and in vivo integration. a, DIC microscopy image of an extracellular microlaser (white arrow) on top of an adult cardiomyocyte. Scale bar, 30 µm. **b**, A magnified view that shows highly organized myofibrils (sarcomere repeat units are indicated by dashed blue lines). Scale bar, 4 µm. **c**, Averaged profiles of n^*_{ext} (black), fluorescent calcium reporter (red) and sarcomere length (SL, blue). The shaded areas represent the s.e.m. of at least ten contractions. Experiments were performed in duplicate for a total of $n = 5$ cells. **d**–**g**, The integration of the microlaser into live zebrafish embryos. **d**, A schematic drawing of microlaser injection. Scale bar, 500 µm. **e**, A brightfield microscopy image of the microlaser attached to the atrium of a zebrafish heart (three days postfertilization (dpf)). Scale bar, 200 µm. **f**, A magnified view of the area indicated by the dashed white box in **e** with the microlaser (arrow). V, ventricle; A, atrium. Scale bar, 50 µm. **g**, Both n_{ext} (red spheres) and n^*_{ext} (blue line) calculated using sensitivity calibration; 2–4 microlasers were injected into three embryos and contraction signals were recorded from three microlasers of one embryo.

contractility, cross-bridge formation and mechanotransduction in individual myofibrils (Supplementary Fig. 9).

Simultaneous sensing of calcium dynamics and contractility

Microlaser contractility measurements can also be combined with all-optical electrophysiology platforms[21,22]. Simultaneous laser spectroscopy and calcium imaging were performed on fully differentiated mouse cardiomyocytes that comprise highly organized myofibrils and a transverse tubular system that ensures synchronized calcium release and rapid contraction throughout the cell (Fig. 5a,b, Supplementary Video 4). Being non-phagocytic, adult cardiomyocytes are not able to actively internalize microlasers, so we instead measured spectral changes in the emission of microlasers that were in contact with the cell membrane. Transient profiles of single electrically paced adult cardiomyocytes again showed contractions as periodic increases in the refractive index (albeit with smaller amplitude than before; Fig. 5c, Supplementary Fig. 10), demonstrating that Δn_{ext} depends on the volume overlap of the evanescent component of the lasing mode with the myofibrils. However, consistent with our previous observation, the refractive index transient showed a direct correlation with sarcomere length (Fig. 5c), which confirms a contraction-induced change in myofibril density. We also compared the contractility profile to the profile of cytosolic Ca^{2+} and found a characteristic latency time of 30 ms between calcium signalling and force development while the maximum contraction speed coincided with peak Ca^{2+} concentration (Fig. 5c).

In vivo integration

Having demonstrated intra- and extracellular sensing in vitro, we next implemented our technique into live zebrafish, a model organism with remarkable capabilities to repair and regenerate large fractions of the heart[23]. Microlasers were injected through a microneedle (Fig. 5d), which led to them being placed at the outer wall of the atrium (Fig. 5e,f). Extracellular sensing rather than direct intracellular injection was performed to avoid disruption of the myocardium which at this developmental stage consists of a single layer of cardiomyocytes that is not yet covered by the developing epicardium[24,25]. Lasing wavelengths again showed the typical redshift associated with cardiomyocyte contraction (Supplementary Fig. 11). Due to increased tissue scattering and rapid movement (Supplementary Video 5), the intensity of individual modes varied strongly and the lower intensity transverse magnetic modes were not detected for a large fraction of the contraction cycle; however, after calibrating the sensitivity of the microlaser from time-points that contained a sufficient number of modes (Supplementary Fig. 12; compare with Fig. 2e), we were able to construct complete contractility profiles for the beating zebrafish heart (Fig. 5g). A measurement performed at a more posterior position of the atrium revealed a significantly longer systolic plateau (Supplementary Fig. 13), demonstrating locally resolved contractility profiles under in vivo conditions.

Deep tissue contractility sensing

The scattering of light in biological tissue severely limits the maximum depth at which optical imaging and sensing can be performed. We performed contractility sensing in preparations of thick, electrically paced myocardial slices to explore the advantages of microlasers over conventional fluorescent probes for deep tissue recording (Fig. 6a). With the ability to maintain functional, contractile heart sections for several months, cardiac slices represent an increasingly important model system for drug screening and for testing of novel cardiac regeneration approaches[26–28]; however, single- and even multiphoton microscopes fail to capture subcellular information from these slices as their typical thicknesses of 0.2–0.5 mm exceed the scattering length of ballistic photons. We recorded two-photon microscopy stacks of heart muscle tissue to illustrate this limitation (Fig. 6b). Although the improved penetration depth at the excitation wavelength of 880 nm enables imaging at considerably larger depths than with conventional confocal microscopy, the image contrast degraded quickly with increasing depth, making it impossible to resolve individual sarcomeres (typical spacing, 2 µm) or cell contours beyond a depth of 100 µm. These results are in agreement with previously published contractility studies where the requirement for fast and high-resolution sampling has so far prevented imaging of cellular features in live heart tissue at depths greater than 100 µm (refs. [1,7]).

We applied microlasers to a series of living myocardial slices with varying thickness between 100 and 400 µm to test whether they can sense contractility of cardiomyocytes at depths beyond the limit of

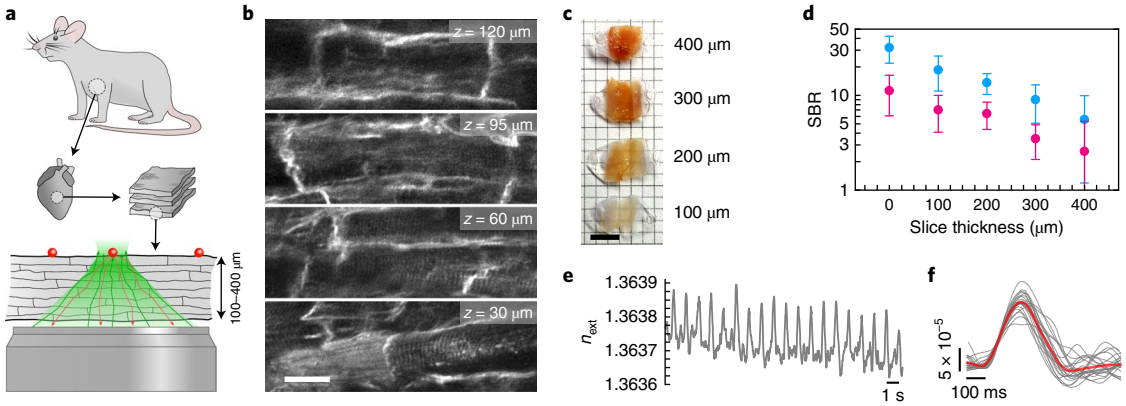

Fig. 6 | Living myocardial slices and deep tissue contractility sensing. a, The preparation of left ventricular slices from adult rat hearts is shown. Microlasers (red spheres) were deposited on top of contracting slices. The excitation of the microlasers (the green arrows illustrate a combination of ballistic and diffuse pump light) through the slice and detection of the microlaser emission (red arrows) by the same objective is shown below. **b**, Two-photon microscopy images of the left ventricle at different imaging depths (z). Scale bar, 20 µm. **c**, A photograph of precision-cut cardiac slices with different thicknesses. Scale bar, 5 mm. **d**, The SBR of microlasers as a function of slice thickness for the most (TE, blue) and least intense (TM, pink) laser modes. The error bars represent the s.e.m. and were obtained by analysing two slices from two hearts and 20 microlasers per thickness. **e**, A n_{ext} profile of a single microlaser recorded through a 350 µm thick cardiac slice that was electrically paced at 1 Hz. **f**, The overlaid profiles (grey) from **e** and the average contractility profile (red) are shown. Experiments were performed in triplicate and contractility profiles have been recorded for $n = 11$ microlasers.

current microscopes (Fig. 6c). We changed to red-emitting lasers ($\lambda = 610$ nm) that are pumped by green light ($\lambda = 540$ nm) to improve light penetration. Although the signal decreased with increasing tissue thickness, sufficient SBRs from two pairs of transverse electric and transverse magnetic modes were obtained to perform full refractive index analysis even through 400 µm thick cardiac slices (Fig. 6d, Supplementary Fig. 14); that is, at a depth that was four times greater than the maximum depth at which multiphoton microscopes can still resolve subcellular features. Following electrical pacing, the slices contracted reproducibly, inducing clearly measurable changes in n_{ext} (Fig. 6e). From this data, we extracted high-resolution contractility profiles (Fig. 6f) that are comparable in quality and amplitude to those detected in isolated cardiomyocytes (compare with Fig. 5c).

Discussion

Restoring cardiac function after severe heart injury remains a major clinical challenge due to the low capacity of the adult mammalian heart to grow new cardiomyocytes[29]. Current regeneration approaches explore the injection of cardiomyocytes derived from human embryonic stem cells or induced pluripotent stem cells into the injured heart and the growth of cardiac tissue in vitro[30–33]. Multifunctional probes that monitor engineered cardiac tissue or the long-term integration of injected cells are urgently needed. Chemical sensing with dye-based or transgenic calcium and voltage reporters are now routinely used for all-optical electrophysiology[24,34]; however, despite their importance, these sensors do not provide insights into the mechanical forces developed by the cells. The processes by which engineered and native cardiac tissue couple mechanically therefore remain unknown[31,35]. Microlaser-based contractility measurements fill this critical gap by monitoring the contractile properties of individual cells during various developmental stages without the need for staining or genetic alteration. Our spectroscopic contractility technique is also resilient to scattering compared to imaging-based methods as scattering in biological tissue is elastic and hence does not alter spectral characteristics. Furthermore, the nanosecond-pulsed pumping in combination with single-shot readout applied here virtually eliminates temporal averaging effects that represent a common source of motion artefacts in intravital confocal or light sheet microscopy[6]. This can be combined with recent advances in focussing of light deep into scattering tissue[36], to achieve remote and non-invasive monitoring of cardiac function in vivo. For the example of cardiac slices shown here, the high sensitivity, bright emission and single-cell specificity of the microlasers leads to better performance at depth than is achievable with state-of-the-art microscopes. We expect that the application of novel microlaser sources that are excited in the near-infrared transparency windows of biological tissue will enable a dramatic further increase in sensing depth[37].

In the future, implementing our recently developed semiconductor WGM nanolasers[14], nanowire lasers[38,39] or plasmonic nanolasers[40,41] will improve and simplify internalization further, eliminate any mechanical restriction of the laser probes and drastically reduce the required pump energy; however, surface passivation, heat management and advanced calibration protocols are needed for these single-mode lasers before a comparable degree of biocompatibility and refractive index sensitivity can be achieved. Furthermore, using high throughput chip-based devices[42] can enable massively parallel integration of lasers into human-embryonic-stem-cell- or induced-pluripotent-stem-cell-derived cardiomyocytes, which in turn would facilitate labelling and monitoring of individual cells from the very early stages of the generation of functional cardiac tissue onwards. Likewise, microlasers can offer functional sensing in newly developed stem cell therapies that are able to restore infarcted tissue[43]. Moreover, techniques developed for ultra-sensitive detection, including quantum-enhanced single-molecule biosensing or frequency comb spectroscopy, might be adopted to increase sensitivity and specificity of intracellular microlaser sensors even further[44–46]. By providing single-cell specificity, long-term tracking, and reduced sensitivity to scattering, microlasers introduce new possibilities for translational approaches that extend well beyond current microscopy-based techniques, offer reduced complexity, and impose fewer experimental restrictions.

Online content

Any methods, additional references, Nature Research reporting summaries, source data, extended data, supplementary information, acknowledgements, peer review information; details of

author contributions and competing interests; and statements of data and code availability are available at https://doi.org/10.1038/s41566-020-0631-z.

Received: 10 April 2019; Accepted: 1 April 2020;
Published online: 15 June 2020

References

1. Aguirre, A. D., Vinegoni, C., Sebas, M. & Weissleder, R. Intravital imaging of cardiac function at the single-cell level. *Proc. Natl Acad. Sci. USA* **111**, 11257–11262 (2014).
2. Kobirumaki-Shimozawa, F. et al. Nano-imaging of the beating mouse heart in vivo: importance of sarcomere dynamics, as opposed to sarcomere length per se, in the regulation of cardiac function. *J. Gen. Physiol.* **147**, 53–62 (2016).
3. Pasqualin, C. et al. SarcOptiM for ImageJ: high-frequency online sarcomere length computing on stimulated cardiomyocytes. *Am. J. Physiol. Physiol.* **311**, C277–C283 (2016).
4. Lind, J. U. et al. Instrumented cardiac microphysiological devices via multimaterial three-dimensional printing. *Nat. Mater.* **16**, 303–308 (2016).
5. Mickoleit, M. et al. High-resolution reconstruction of the beating zebrafish heart. *Nat. Methods* **11**, 919–922 (2014).
6. Vinegoni, C., Lee, S., Aguirre, A. D. & Weissleder, R. New techniques for motion-artifact-free in vivo cardiac microscopy. *Front. Physiol.* **6**, 147 (2015).
7. Matsuura, R. et al. Intravital imaging with two-photon microscopy reveals cellular dynamics in the ischeamia-reperfused rat heart. *Sci. Rep.* **8**, 15991 (2018).
8. Liu, R., Li, Z., Marvin, J. S. & Kleinfeld, D. Direct wavefront sensing enables functional imaging of infragranular axons and spines. *Nat. Methods* **16**, 615–618 (2019).
9. Vollmer, F. & Arnold, S. Whispering-gallery-mode biosensing: label-free detection down to single molecules. *Nat. Methods* **5**, 591–596 (2008).
10. Kim, E., Baaske, M. D., Schuldes, I., Wilsch, P. S. & Vollmer, F. Label-free optical detection of single enzyme-reactant reactions and associated conformational changes. *Sci. Adv.* **3**, e1603044 (2017).
11. Schubert, M. et al. Lasing within live cells containing intracellular optical microresonators for barcode-type cell tagging and tracking. *Nano Lett.* **15**, 5647–5652 (2015).
12. Humar, M. & Yun, S. H. Intracellular microlasers. *Nat. Photon.* **9**, 572–576 (2015).
13. Schubert, M. et al. Lasing in live mitotic and non-phagocytic cells by efficient delivery of microresonators. *Sci. Rep.* **7**, 40877 (2017).
14. Fikouras, A. H. et al. Non-obstructive intracellular nanolasers. *Nat. Commun.* **9**, 4817 (2018).
15. Martino, N. et al. Wavelength-encoded laser particles for massively multiplexed cell tagging. *Nat. Photon.* **13**, 720–727 (2019).
16. Liu, P. Y. et al. Cell refractive index for cell biology and disease diagnosis: past, present and future. *Lab Chip* **16**, 634–644 (2016).
17. Irving, T. C., Konhilas, J., Perry, D., Fischetti, R. & de Tombe, P. P. Myofilament lattice spacing as a function of sarcomere length in isolated rat myocardium. *Am. J. Physiol. Circ. Physiol.* **279**, H2568–H2573 (2000).
18. Yagi, N. et al. Sarcomere-length dependence of lattice volume and radial mass transfer of myosin cross-bridges in rat papillary muscle. *Pflugers Arch. Eur. J. Physiol.* **448**, 153–160 (2004).
19. Moeendarbary, E. et al. The cytoplasm of living cells behaves as a poroelastic material. *Nat. Mater.* **12**, 253–261 (2013).
20. Schreckenberg, R. in *Cardiomyocytes—Active Players in Cardiac Disease* 135–163 (Springer International, 2016). https://doi.org/10.1007/978-3-319-31251-4_5.
21. Klimas, A. et al. OptoDyCE as an automated system for high-throughput all-optical dynamic cardiac electrophysiology. *Nat. Commun.* **7**, 11542 (2016).
22. Dempsey, G. T. et al. Cardiotoxicity screening with simultaneous optogenetic pacing, voltage imaging and calcium imaging. *J. Pharmacol. Toxicol. Methods* **81**, 240–250 (2016).
23. Cao, J. & Poss, K. D. Explant culture of adult zebrafish hearts for epicardial regeneration studies. *Nat. Protoc.* **11**, 872–881 (2016).
24. Weber, M. et al. Cell-accurate optical mapping across the entire developing heart. *Elife* **6**, e28307 (2017).
25. Brown, D., Samsa, L., Qian, L. & Liu, J. Advances in the study of heart development and disease using zebrafish. *J. Cardiovasc. Dev. Dis.* **3**, 13 (2016).
26. Watson, S. A. et al. Preparation of viable adult ventricular myocardial slices from large and small mammals. *Nat. Protoc.* **12**, 2623–2639 (2017).
27. Watson, S. A. et al. Biomimetic electromechanical stimulation to maintain adult myocardial slices in vitro. *Nat. Commun.* **10**, 2168 (2019).
28. Fischer, C. et al. Long-term functional and structural preservation of precision-cut human myocardium under continuous electromechanical stimulation in vitro. *Nat. Commun.* **10**, 117 (2019).
29. Vujic, A. et al. Exercise induces new cardiomyocyte generation in the adult mammalian heart. *Nat. Commun.* **9**, 1659 (2018).
30. Tzahor, E. & Poss, K. D. Cardiac regeneration strategies: staying young at heart. *Science* **356**, 1035–1039 (2017).
31. Shiba, Y. et al. Allogeneic transplantation of iPS cell-derived cardiomyocytes regenerates primate hearts. *Nature* **538**, 388–391 (2016).
32. Ronaldson-Bouchard, K. et al. Advanced maturation of human cardiac tissue grown from pluripotent stem cells. *Nature* **556**, 239–243 (2018).
33. Liu, Y.-W. et al. Human embryonic stem cell–derived cardiomyocytes restore function in infarcted hearts of non-human primates. *Nat. Biotechnol.* **36**, 597–605 (2018).
34. Jones, J. S., Small, D. M. & Nishimura, N. In vivo calcium imaging of cardiomyocytes in the beating mouse heart with multiphoton microscopy. *Front. Physiol.* **9**, 969 (2018).
35. Gaetani, R. et al. Epicardial application of cardiac progenitor cells in a 3D-printed gelatin/hyaluronic acid patch preserves cardiac function after myocardial infarction. *Biomaterials* **61**, 339–348 (2015).
36. Jeong, S. et al. Focusing of light energy inside a scattering medium by controlling the time-gated multiple light scattering. *Nat. Photon.* **12**, 277–283 (2018).
37. Fernandez-Bravo, A. et al. Continuous-wave upconverting nanoparticle microlasers. *Nat. Nanotechnol.* **13**, 572–577 (2018).
38. Feng, C. et al. Organic-nanowire–SiO_2 core–shell microlasers with highly polarized and narrow emissions for biological imaging. *ACS Appl. Mater. Interfaces* **9**, 7385–7391 (2017).
39. Wu, X. et al. Nanowire lasers as intracellular probes. *Nanoscale* **10**, 9729–9735 (2018).
40. Hill, M. T. & Gather, M. C. Advances in small lasers. *Nat. Photon.* **8**, 908–918 (2014).
41. Ma, R.-M. & Oulton, R. F. Applications of nanolasers. *Nat. Nanotechnol.* **14**, 12–22 (2019).
42. Wu, Y.-C. et al. Massively parallel delivery of large cargo into mammalian cells with light pulses. *Nat. Methods* **12**, 439–444 (2015).
43. Lee, A. S. et al. Prolonged survival of transplanted stem cells after ischaemic injury via the slow release of pro-survival peptides from a collagen matrix. *Nat. Biomed. Eng.* **2**, 104–113 (2018).
44. Mauranyapin, N. P., Madsen, L. S., Taylor, M. A., Waleed, M. & Bowen, W. P. Evanescent single-molecule biosensing with quantum-limited precision. *Nat. Photon.* **11**, 477–481 (2017).
45. Kippenberg, T. J., Holzwarth, R. & Diddams, S. A. Microresonator-based optical frequency combs. *Science* **332**, 555–559 (2011).
46. Coddington, I., Newbury, N. & Swann, W. Dual-comb spectroscopy. *Optica* **3**, 414 (2016).

Methods

Animals. The use of experimental animals was approved by the Animal Ethics Committee of the University of St Andrews and the University of Edinburgh. The care and sacrifice of the animals used conformed to Directive 2010/63/EU of the European Parliament on the protection of animals used for scientific purposes as well as the United Kingdom Animals (Scientific Procedures) Act 1986.

Cell culture. HL-1 cells were cultured in Claycomb medium (Sigma-Aldrich) supplemented with 100 µM norepinephrine, 10% (v/v) foetal bovine serum (FBS), 2 mM L-glutamine and 1% (v/v) penicillin/streptomycin. The cells were stored in T-25 flasks (Fisher Scientific) and incubated at 37 °C with 5% CO_2. Before seeding, the flasks were coated with gelatine/fibronectin (0.02% gelatine, 1 mg ml^{-1} fibronectin) for at least an hour to improve the adherence of the cells. Cells were supplied daily with 1 ml of medium per 3.5 cm^2 of culture area to maintain and maximize the contractile activity.

Isolation and culture of neonatal cardiomyocytes. Neonatal mouse hearts were obtained from postnatal day two to three C57 laboratory mice. Tissue was collected, cleaned and cut into pieces in ice-cold calcium- and magnesium-free Dulbecco's phosphate-buffered saline and digested for 30 min in papain (ten units per millilitre, Worthington) at 37 °C. The treated tissue was dissociated to a single-cell suspension by gentle reverse pipetting in cell culture medium (Dulbecco's Modified Eagle's Medium with 25 mM glucose and 2 mM Glutamax, 10% (v/v) FBS, 1% (v/v) non-essential amino acids, 1% (v/v) penicillin/streptomycin). Non-disaggregated material was allowed to sediment for 2 min and the cell suspension pelleted by centrifugation at ×200 *g* for 5 min. Pelleted cells were resuspended in cell culture medium and pre-plated on an uncoated cell culture flask for 2–4 h to enrich cardiomyocytes through surface attachment of fibroblasts. The cell culture medium that contained unattached cells was then recovered from this flask, cardiomyocytes concentrated by centrifugation and seeded at a density of 2×10^5 cells per dish. Before seeding, culture dishes (Ibidi) were coated with 0.02% gelatin per 5 µg ml^{-1} fibronectin. Cultures were kept in a humidified incubator at 37 °C, 5:95% CO_2:air; 1×10^5 microlasers were added to the dish one day after seeding and incubated overnight. Lasing experiments were performed within the next one to two days while cultures showed widespread spontaneous contractions for up to two weeks.

Isolation of adult cardiomyocytes. Adult cardiomyocytes were isolated using an adapted Langendorff-free protocol, as previously described in ref. [47]. Isolation solutions used were based on a modified Tyrode's solution: ethylenediaminetetraaceticacid (EDTA) buffer, 5 mM KCl, 130 mM NaCl, 0.5 mM NaH_2PO_4, 10 mM HEPES, 10 mM glucose, 5 mM sodium-pyruvate and 5 mM EDTA titrated to pH 7.8 with NaOH; perfusion buffer, 5 mM KCl, 130 mM NaCl, 0.5 mM NaH_2PO_4, 10 mM HEPES, 10 mM glucose, 5 mM sodium-pyruvate and 1 mM $MgCl_2$ titrated to pH 7.8 with NaOH; collagenase buffer, 35 mg collagenase type II (Worthington), 50 mg BSA and 15 mg protease (type XIV, Sigma-Aldrich) diluted in 30 ml of perfusion buffer.

Adult C57 mice were killed by cervical dislocation, the chest cavity rapidly opened and descending vessels severed. The right ventricle was injected with 7 ml of EDTA buffer over 1 min to quickly clear residual blood and stop contraction. The ascending aorta was clamped in situ using haemostatic forceps and the heart excised. The heart was then submerged in EDTA buffer, with a further 10 ml injection of EDTA buffer into the left ventricle over 3 min. EDTA buffer was cleared by injection of 3 ml of perfusion buffer into the left ventricle. The heart was then submerged in collagenase buffer and 30–50 ml of collagenase buffer was injected into the left ventricle over 10 min. Digestion was considered complete following a marked reduction in resistance to injection pressure. The digested heart was then transferred to a culture dish containing fresh collagenase buffer and trimmed of any excess non-cardiac tissue. Cardiomyocyte dissociation was completed by gentle trituration using a P1000 pipette. Enzymatic digestion was inhibited by addition of perfusion buffer containing 5% (v/v) FBS (ThermoFisher). Isolated cardiomyocytes were reintroduced to Ca^{2+} by three rounds of 20 min sequential gravity settling in perfusion buffer containing 300 µM, 500 µM and 1 mM $CaCl_2$, respectively. Cells were stained (see below) and subsequently transferred into a culture dish (Ibidi) containing 1 mM Ca^{2+} perfusion buffer. After the cells sedimented, 1×10^4 microlasers were added to the dish and lasing experiments were performed within 3 h of isolation.

Cardiomyocyte staining. Neonatal cardiomyocytes were labelled with 100 nM SiR-actin overnight. Following isolation, adult cardiomyocytes were loaded with 10 µM X-Rhod-1 AM ($\lambda_{ex}=580$ nm, $\lambda_{em}=602$ nm; Thermo Fisher) in perfusion buffer containing 1 mM $CaCl_2$ for 45 min at room temperature. Cells were then washed in 1 mM Ca^{2+} perfusion buffer and left for 15 min at room temperature to allow de-esterification of X-Rhod-1 AM.

Microlasers. 15 µm diameter polystyrene–divinylbenzene microspheres stained with Firefli Fluorescent Green (Thermo Fisher, 11895052, coefficient of variance (CV) < 12%, excitation/emission maximum: 468 nm/508 nm) were used in all experiments, except for cardiac slices where 15.5 µm diameter polystyrene microspheres with red emission (MicroParticles GMBH, PS-FluoRed-15.5, CV 2%, excitation/emission maximum: 530 nm/607 nm) were used.

Laser spectroscopy. All components for optical pumping and laser spectroscopy were integrated into a standard inverted fluorescence microscope (Nikon, TE2000), equipped with epifluorescence and DIC. The output from a Q-switched diode-pumped solid-state laser (Alphalas)—with a wavelength, pulse width and repetition rate of 473 nm, 1.5 ns and 100 Hz, respectively—was coupled into the objective via a dichroic filter and passed to the sample through either a ×60 oil immersion (Nikon CFI Plan Apo VC, NA 1.4) or a ×40 (Nikon, Plan Apo, NA 0.95) objective. In addition, a further ×1.5 magnification was used for sarcomere length tracking. The pump laser was focussed to a 15 µm large spot and a maximum pulse energy of 1–50 nJ was used depending on resonator size and tissue scattering. Emission from the microlaser was collected by the same objective, separated from the pump light by the dichroic and passed to the camera port of the microscope. The image was relayed to a 300 mm spectrometer (Andor Shamrock 303i with a 1,800 lines per mm grating and Andor Newton DU970P-BVF) and a cooled sCMOS camera (Hamamatsu, Orca Flash 4.0v2) using a series of relay lenses and dichroic beam splitters. The pump laser and spectrometer were synchronized such that each spectrum corresponded to a single pump pulse (acquisition rate, 100 Hz). We note that in the single-pulse excitation and single-pulse collection scheme applied here, the acquisition rate can be further increased by increasing both the laser repetition frequency and spectrometer acquisition rate. During lasing experiments, cells were kept in a humidified on-stage incubator system (Bioscience Tools) set to 37 °C and purged with 5:95% CO_2:air.

Laser threshold characteristics were acquired on the same set-up by varying the pump power with a set of neutral density filters. Spectra were integrated over 800 pump pulses below the threshold, whereas between 100 and 20 pump pulses were used above the threshold. The SBR is defined as SBR $= \frac{I_{WGM}-I_{BG}}{I_{BG}}$, where I_{WGM} is the laser mode peak intensity and I_{BG} is the average background intensity in a 1 nm window around the laser mode. SBR measurements were performed by integrating over only one pump pulse to resemble the conditions of the cardiac measurements; 100 spectra were analysed for each pump energy.

Cardiac slices were measured on the same microscope. Red-emitting microlasers were pumped by an optical parametric amplifier tuned to 540 nm (Ekspla, 26 ps pulse width, 1 kHz repetition rate) through a ×20 objective (Nikon, CFI Plan Fluor, NA 0.45). Here the acquisition rate of the spectrometer was 50 Hz. SBR was determined as above, analysing 500 spectra for each microlaser. Contractility data in thick slices were obtained by smoothing (Savitzky–Golay, 15 points, second order) the fitted laser mode time traces before application of the refractive index fitting algorithm.

Confocal microscopy. Confocal imaging was performed on a Leica TCS SP8 laser scanning microscope with ×40 and ×63 oil immersion objectives. Neonatal cardiomyocytes were fixed for 10 min in 4% paraformaldehyde, permeabilized with Triton X-100 (1 h) and subsequently incubated with the primary cardiac troponin T monoclonal antibody (overnight at 4 °C) (Thermo Fisher, MA5-12960), the secondary Anti-Mouse IgG CF 594 antibody (1 h) (Sigma-Aldrich, SAB4600092) and 4′,6-diamidino-2-phenylindole; 4′,6-diamidino-2-phenylindole, microlasers and myofibrils were excited by sequentially scanned continuous-wave lasers with a wavelength of 405 nm, 488 nm and 594 nm, respectively.

Multiphoton microscopy. Imaging was carried out on a Zeiss LSM 710 confocal/multiphoton system based on a Zeiss AXIO Observer Z1 inverted microscope equipped with a Plan-Apochromat ×20 NA 0.8 objective. Confocal imaging used a 543 nm continuous-wave laser and multiphoton imaging a Coherent Chameleon laser tuned to 880 nm. The sample was stained by Langendorff perfusion of an adult rat heart with a 100 µM solution of the membrane dye Di-2-ANEPEQ (PromoCell, PK-CA707-61013) for 30 min at room temperature, followed by dissection of the left ventricle and subsequent imaging[1]. The power of the multiphoton laser was increased with increasing imaging depth.

Multimodal imaging. In addition to the laser coupling spectroscopy optics, a red bandpass filter placed in the dia illumination path of the microscope, a quad-edge epiluminescence filter cube and additional band pass filters at the spectrograph and camera allowed simultaneous recording of microlaser lasing spectra, and the epifluorescence and DIC imaging of cells. Live cell imaging was performed by using an on-stage incubator system.

Sarcomere length measurements. To determine the average sarcomere length in neonatal mouse cardiomyocytes, myofibrils were fluorescently labelled with SiR-actin (see above) and videos were recorded under epi-illumination conditions at 50 fps using a ×60 oil immersion objective (NA 1.4). Raw fluorescence microscopy images were first smoothed by removing statistical noise[48]. From the smoothed videos intensity profiles were taken along individual myofibrils, covering 5–8 sarcomere units. Profiles were then interpolated by a factor of ten to facilitate an increase in the spatial resolution of the length measurements to about 10 nm that was otherwise limited by the pixel size of the camera and magnification of the microscope. Interpolated profiles were smoothed using the Savitzky–Golay

method. Minima in the intensity profiles were tracked through time at 20 ms intervals. Once the separation between the first and last minima was determined, it was divided by the number of sarcomeres to calculate the average sarcomere length in each frame. In adult cardiomyocytes, sarcomere length measurements were performed using DIC videos recorded at 100 fps by using the ImageJ plugin SarcOptiM[3]. Briefly, a fast Fourier transformation algorithm is used to extract the regular spacing in a line profile plotted along the longitudinal axis of the cell. Adult cardiomyocytes were electrically paced at 1 Hz with Platinum wire bath electrodes by applying 8 ms square voltage pulses with a maximum electric field of 30 V cm^{-1}.

In vivo zebrafish experiments. All zebrafish embryos used in our experiments were under the age of 5 dpf. Embryos were collected from random matings and then correctly developmentally staged. Fertilized eggs were transferred at the 2–8 cell stage to 10 cm culture dishes at 28.5 °C with systems water replaced every 24 h. When necessary, larvae were anaesthetized with tricaine methanesulfonate (40 μg ml^{-1}, Sigma-Aldrich). Microlasers were injected into the sinus venosus region of 3 dpf embryos with a micropipette (pulled on a Sutter P97) attached to a Narishige IM-300 microinjector, while viewed on a stage of a Leica M16F stereo microscope. Lasing experiments were performed at room temperature.

Cardiac slices. Cardiac slices were prepared from rat hearts following previously described methods[26,28].

Experimental solutions were as follows: slicing solution, 30 mM BDM, 140 mM NaCl, 6 mM KCl, 10 mM glucose, 1 mM $MgCl_2$, 1.8 mM $CaCl_2$, 23 mM $NaHCO_3$ titrated to 7.4 with HCl; Tyrode's solution, 140 mM NaCl, 5 mM KCl, 10 mM glucose, 1 mM $MgCl_2$, 2 mM $CaCl_2$, 23 mM $NaHCO_3$ titrated to 7.4 with HCl. Solutions were filtered with 0.22 μm filter (Millipore) and cooled to 4 °C. Carbogen gas (95:5% O_2:CO_2) was used to bubble solutions throughout the preparation and slicing of the heart.

Adult Wistar rats were anesthetized by Pentobarbital injection, sacrificed by cervical dislocation and death confirmed by carotid artery dissection. The chest cavity was opened and the vessels cut. The heart and lungs were removed from the animal, submerged in cold slicing solution and blood ejected from the heart by compressing for 10–15 s. Heart and lungs were transferred to a 10 cm dish (Fisher) filled with cold slicing solution. Using a scalpel, the lungs were dissected off, followed by the atria and right ventricle. An incision was made down the septum towards the apex, the ventricle opened, papillary muscles removed and tissue block flattened. Excess solution was blotted from the epicardial surface, and the tissue block attached to a block of 3.5% agar (3.5% agar made in dH_2O) using superglue, with the epicardial surface face down. The agar block was then glued to the specimen holder and set in the vibratome bath so the ventricle was sliced from base to apex. The vibratome bath was filled with cold slicing solution until the tissue block was fully covered.

Slicing was carried out on Leica VT 1200 vibratome using a stainless steel blade (Wilkinson Sword), which was replaced for each ventricular block. The settings were as follows: 2 mm amplitude, blade advance of 0.03 mm s^{-1}. The slice thickness was varied between 100–400 μm. Once the slice detached from the tissue block, a fine brush was used to transfer the sample to a well of a six-well plate (Fisher) filled with 4 °C Tyrode's solution. The slice was flattened and held down with gauze and a metal washer and the plate kept on ice.

Reporting summary. Further information on research design is available in the Nature Research Reporting Summary linked to this article.

Data availability

The research data underpinning this publication can be accessed at https://doi.org/10.17630/97927f1f-a111-46d0-8d41-038771733b73 (ref. [49]).

Code availability

The custom-made computer code is available at https://doi.org/10.17630/97927f1f-a111-46d0-8d41-038771733b73 (ref. [49]).

References

47. Ackers-Johnson, M. et al. A simplified, Langendorff-free method for concomitant isolation of viable cardiac myocytes and nonmyocytes from the adult mouse heart. *Circ. Res.* **119**, 909–920 (2016).
48. Carlton, P. M. et al. Fast live simultaneous multiwavelength four-dimensional optical microscopy. *Proc. Natl Acad. Sci. USA* **107**, 16016–16022 (2010).
49. Schubert, M. et al. Monitoring contractility in cardiac tissue with cellular resolution using biointegrated microlasers (dataset). *Univ. St Andrews Res. Portal* https://doi.org/10.17630/97927f1f-a111-46d0-8d41-038771733b73 (2020).

Acknowledgements

We thank S. A. Sharples for assistance with the preparation of myocardial slices. This research was financially supported by the European Research Council under the European Union's Horizon 2020 Framework Programme (FP/2014-2020)/ERC grant agreement no. 640012 (ABLASE), by EPSRC (grant no. EP/P030017/1) and by the RS Macdonald Charitable Trust. S.J.P. acknowledges funding by the Royal Society of Edinburgh (Biomedical Fellowship) and the British Heart Foundation (grant no. FS/17/9/32676). S.J.P. and G.B.R. acknowledge support from The Wellcome Trust Institutional Strategic Support Fund to the University of St Andrews (grant no. 204821/Z/16/A). M.S. acknowledges funding by the European Commission (Marie Skłodowska-Curie Individual Fellowship, 659213) and the Royal Society (Dorothy Hodgkin Fellowship, DH160102; grant no. RGF\R1\180070).

Author contributions

M.S. designed, performed and analysed laser experiments and imaging. L.W. contributed to lasing experiments and B.C. contributed to sarcomere length measurements. I.R.M.B. and L.W. developed refractive index fitting and peak fitting software, respectively. A.M. and M.S. prepared neonatal cardiomyocyte cultures with support from G.B.M. G.B.R. prepared isolated cardiomyocytes and A.M.D. prepared cardiac slices under supervision of S.J.P. S.J.P. and M.S. designed physiological experiments in isolated cardiomyocytes and cardiac slices. C.S.T. supported the preparation of zebrafish. P.L.A. performed two-photon microscopy. M.S. and M.C.G. conceived the project and wrote the manuscript with contributions from all authors.

Competing interests

The authors declare no competing interests.

Additional information

Supplementary information is available for this paper at https://doi.org/10.1038/s41566-020-0631-z.

Correspondence and requests for materials should be addressed to M.S. or M.C.G.

Reprints and permissions information is available at www.nature.com/reprints.

nature research

Corresponding author(s): Marcel Schubert, Malte C Gather

Last updated by author(s): Mar 13, 2020

Reporting Summary

Nature Research wishes to improve the reproducibility of the work that we publish. This form provides structure for consistency and transparency in reporting. For further information on Nature Research policies, see Authors & Referees and the Editorial Policy Checklist.

Statistics

For all statistical analyses, confirm that the following items are present in the figure legend, table legend, main text, or Methods section.

n/a	Confirmed
☐	☒ The exact sample size (*n*) for each experimental group/condition, given as a discrete number and unit of measurement
☒	☐ A statement on whether measurements were taken from distinct samples or whether the same sample was measured repeatedly
☒	☐ The statistical test(s) used AND whether they are one- or two-sided *Only common tests should be described solely by name; describe more complex techniques in the Methods section.*
☒	☐ A description of all covariates tested
☒	☐ A description of any assumptions or corrections, such as tests of normality and adjustment for multiple comparisons
☒	☐ A full description of the statistical parameters including central tendency (e.g. means) or other basic estimates (e.g. regression coefficient) AND variation (e.g. standard deviation) or associated estimates of uncertainty (e.g. confidence intervals)
☒	☐ For null hypothesis testing, the test statistic (e.g. *F*, *t*, *r*) with confidence intervals, effect sizes, degrees of freedom and *P* value noted *Give P values as exact values whenever suitable.*
☒	☐ For Bayesian analysis, information on the choice of priors and Markov chain Monte Carlo settings
☒	☐ For hierarchical and complex designs, identification of the appropriate level for tests and full reporting of outcomes
☒	☐ Estimates of effect sizes (e.g. Cohen's *d*, Pearson's *r*), indicating how they were calculated

Our web collection on statistics for biologists contains articles on many of the points above.

Software and code

Policy information about availability of computer code

Data collection	DIC, fluorescence, confocal and 2-photon microscopy images acquired with Hamamatsu HCImage 4.6.0, Leica LAS-X, and Zeiss ZEN. Spectroscopic data acquired with Andor Solis.
Data analysis	Data analysis was performed with OriginPro 2017-2019, FIJI (based on ImageJ 1.52p), and Matlab 2016-2019. The custom-made computer code is available at https://doi.org/10.17630/97927f1f-a111-46d0-8d41-038771733b73

For manuscripts utilizing custom algorithms or software that are central to the research but not yet described in published literature, software must be made available to editors/reviewers. We strongly encourage code deposition in a community repository (e.g. GitHub). See the Nature Research guidelines for submitting code & software for further information.

Data

Policy information about availability of data

All manuscripts must include a data availability statement. This statement should provide the following information, where applicable:

- Accession codes, unique identifiers, or web links for publicly available datasets
- A list of figures that have associated raw data
- A description of any restrictions on data availability

The research data underpinning this publication can be accessed at https://doi.org/10.17630/97927f1f-a111-46d0-8d41-038771733b73.

Field-specific reporting

Please select the one below that is the best fit for your research. If you are not sure, read the appropriate sections before making your selection.

☒ Life sciences ☐ Behavioural & social sciences ☐ Ecological, evolutionary & environmental sciences

Life sciences study design

All studies must disclose on these points even when the disclosure is negative.

Sample size	Sample size was at least greater than n=10 for experiments of exploratory nature (e.g. n>150 cells were analysed that revealed the increased refractive index upon cardiac contraction and n=12 cells were analysed for establishing the correlation between myofibril contractility and refractive index change). All other experiments have sample sizes greater than n=3 and several repeats except for zebrafish experiments. Zebrafish laser injection was performed in n=3 samples but lasing measurements were performed on only one which is sufficient for a proof of concept study given the previously established correlations. The sample size is stated in the Methods section, Figure Legends, or Main text for each measurement.
Data exclusions	Microlaser without significant wavelength shift (typically smaller than 1-5 pm) or with strongly distorted contractility profiles were not analysed.
Replication	All experiments were performed with biological replicates. The number of repeats is stated in the Methods section, Figure Legends, or Main text. All experimental findings were reliably reproduced.
Randomization	Randomization of animals was not required as no comparisons between groups has been performed.
Blinding	No blinding has been applied as the study does not contain comparisons between different sample groups or required data analysis that is affected by experience or subjective interpretation of a particular researcher.

Reporting for specific materials, systems and methods

We require information from authors about some types of materials, experimental systems and methods used in many studies. Here, indicate whether each material, system or method listed is relevant to your study. If you are not sure if a list item applies to your research, read the appropriate section before selecting a response.

Materials & experimental systems

n/a	Involved in the study
☐	☒ Antibodies
☐	☒ Eukaryotic cell lines
☒	☐ Palaeontology
☐	☒ Animals and other organisms
☒	☐ Human research participants
☒	☐ Clinical data

Methods

n/a	Involved in the study
☒	☐ ChIP-seq
☒	☐ Flow cytometry
☒	☐ MRI-based neuroimaging

Antibodies

Antibodies used	Primary cardiac troponin T (cTnT) monoclonal antibody (Thermo Fisher, UK, MA5-12960); secondary Anti-Mouse IgG CF™ 594 antibody (Sigma-Aldrich, SAB4600092).
Validation	cTnT primary antibody was verified by relative expression by the manufacturer and the antiboday has been cited in 126 references at the time of manuscript submission. The secondary antibody has been confirmed by strong fluorescence of the conjugated dye and the selective staining of known cellular structures (myofibrils).

Eukaryotic cell lines

Policy information about cell lines

Cell line source(s)	HL-1 cardiac cells were purchased from Sigma-Aldrich.
Authentication	Cells were used as purchased and no additional authentication checks were performed.
Mycoplasma contamination	The cell line was not tested for mycoplasma contamination during the course of this study. However, testing on a regular basis is performed in the lab.
Commonly misidentified lines (See ICLAC register)	No commonly misidentified cell lines have been used in this study.

Animals and other organisms

Policy information about studies involving animals; ARRIVE guidelines recommended for reporting animal research

Laboratory animals	Adult and neonatal C57 mice, adult Wistar rats, and a maximum of 5 days old zebrafish (Danio rerio).
Wild animals	The study did not involve wild animals.
Field-collected samples	The study did not involve field-collected samples.
Ethics oversight	The use of experimental animals was approved by the Animal Ethics Committee of the University of St Andrews and the University of Edinburgh. The care and sacrifice of animals used conformed to Directive 2010/63/EU of the European Parliament on the protection of animals used for scientific purposes as well as the United Kingdom Animals (Scientific Procedures) Act 1986.

Note that full information on the approval of the study protocol must also be provided in the manuscript.